Static analysis of functionally graded beams using higher order shear deformation theory

Ravikiran Kadoli [a,*], Kashif Akhtar [a], N. Ganesan [b]

[a] *Department of Mechanical Engineering, National Institute of Technology Karnataka, Srinivasnagar 575 025, India*
[b] *Department of Mechanical Engineering, Indian Institute of Technology Madras, Chennai 600 036, India*

Abstract

Displacement field based on higher order shear deformation theory is implemented to study the static behavior of functionally graded metal–ceramic (FGM) beams under ambient temperature. FGM beams with variation of volume fraction of metal or ceramic based on power law exponent are considered. Using the principle of stationary potential energy, the finite element form of static equilibrium equation for FGM beam is presented. Two stiffness matrices are thus derived so that one among them will reflect the influence of rotation of the normal and the other shear rotation. Numerical results on the transverse deflection, axial and shear stresses in a moderately thick FGM beam under uniform distributed load for clamped–clamped and simply supported boundary conditions are discussed in depth. The effect of power law exponent for various combination of metal–ceramic FGM beam on the deflection and stresses are also commented. The studies reveal that, depending on whether the loading is on the ceramic rich face or metal rich face of the beam, the static deflection and the static stresses in the beam do not remain the same.
© 2007 Elsevier Inc. All rights reserved.

Keywords: Rotation of the normal; Shear rotation; Functionally graded metal–ceramic beam; Transverse displacement; Stresses

1. Introduction

The technique of grading ceramics along with metals initiated by the Japanese material scientist in Sendai has marked the beginning of exploring the possibility of using FGMs for various structural applications [1]. Undoubtedly, FGM are meant for use where temperature fluctuations are severe. However, their performance for loads under ambient conditions is also necessary to be investigated since, there can exist situations where temperature fluctuations may be present for a short duration. Hence it is essential to examine the static behavior of rectangular FGM beams, in terms of transverse deflection, transverse shear strain and stresses. During the last two decade there has been a considerable research reports on thermal stresses, fracture, thermomechanical response, buckling, free vibration, etc. of FGM structural elements.

---

* Corresponding author.
  E-mail address: rkkadoli@rediffmail.com (R. Kadoli).

The literature reveals a continued interest among the research community to develop efficient mathematical models to predict the static and dynamic response of thin and thick beams. Kapania and Raciti [2] provide a detailed review of shear deformation theories used for the static, vibration and buckling analysis of beams and plates. Shi et al. [3] presented the quasi-conforming finite element for the deflection analysis of composite beams using higher order theory. Chakraborty et al. [4] developed an exact shear deformable beam finite element to study the static, free vibration, and wave propagation problems for bi-material beams fused with FGM. Sankar and Tzeng [5] obtained an elasticity solution for FGM beams with exponential variation of properties subjected to transverse loads. Subsequently, Sankar [6] developed a beam theory similar to simple Euler–Bernoulli beam theory for functionally graded beams with elastic properties to vary exponentially and evaluated thermal stresses. Calio and Elishakoff [7] derived closed form solutions for the natural frequencies of axially graded beam-columns on elastic foundations with guided end conditions. Wu et al. [8] demonstrates the use of semi-inverse method to find the solutions to the dynamic equation of axially functionally graded simply supported beams. Croce and Venini [9] formulated the governing equations for the behavior of Reissner–Mindlin FGM plates. Zenkour [10] has derived the exact solution for FGM plates using generalized sinusoidal shear deformation theory and presented numerical results on displacement and stress response of FGM plates under uniform loading. A general two-dimensional solution for the static analysis of a cantilever orthotropic functionally graded beam using Airy stress function has been presented by Zhong and Yu [11]. Ding et al. [12] have derived partial differential equation for plane stress problem of generally anisotropic beams and stress functions thereof to obtain elasticity solution for anisotropic FGM beams with various boundary conditions. Two-dimensional analytical solutions for orthotropic beams have been solved using two harmonic displacement functions and Airy stress function respectively by Jiang and Ding [13] and Ding et al. [14]. Vibration and instability of spinning and stationary thin walled beams made functionally graded materials was investigated under temperature gradients and high temperature based on thermo-elastic modeling by Oh et al. [15], Librescu et al. [16] and Librescu and Oh [17]. Nonlinear static analysis of unsymmetrical functionally graded thin beams with geometric nonlinearity was investigated by Deschilder et al. [18].

The literature survey gives a clear indication that studies on static deflection and stresses under ambient loading conditions of metal–ceramic FGM beams using higher order shear deformation theory are very few in numbers, hence the objective of the present paper. Kinematics for moderately thick rectangular beams satisfying zero shear strain on the top and bottom surfaces is utilized to define the strain displacement relation involving the membrane, bending, higher order displacement and transverse shear strain. Independent strain energies containing rotation of the normal and shear rotation terms are deduced. The principle of stationary potential energy is used to obtain the static finite element equilibrium equations for FGM (functionally graded material) beam with uniformly distributed transverse load. Equivalent single layer approach is followed for the evaluation of the constitutive matrix of the FGM beam. The finite element formulation follows the conventional displacement based approach to derive the stiffness matrices. Deflection and stress distribution in a moderately thick FGM beam with various metal ceramic combination subjected to uniform load intensity are presented.

2. Material properties of FGM beam and finite element formulation

2.1. Effective material properties of metal ceramic functionally graded beams

Fig. 1 shows a FGM beam composed of ceramic and metal of length L, width b and thickness h. Material properties vary continuously in the z direction. Topmost surface consists of only metal and bottom surface has only ceramic. In between volume fraction of ceramic V_c and metal V_m are obtained by power law distribution in conjunction with simple law of constituent mixture as follows:

$$V_c = \left(\frac{z}{h} + \frac{1}{2}\right)^n, \tag{1a}$$
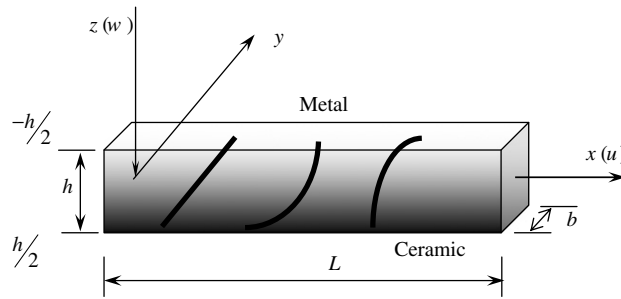
$$V_m = 1 - V_c, \tag{1b}$$

Fig. 1. Geometry of FGM beam and the possible variation of ceramic and metal through thickness.

where z = distance from mid-surface and n = power law index, a positive real number. For $n = 0$ volume fraction of ceramic becomes one and homogeneous beam consisting only ceramic is obtained. When value of n is increased, content of metal in FGM increases. The effective material properties MP_{eff} are evaluated using the relation,

$$MP_{eff}(z) = MP_m V_m(z) + MP_c V_c(z),$$ (2)

where MP_m and MP_c stands for material properties of metals and ceramics respectively. Thus the modulus of elasticity E_{eff}, Poisson's ratio v_{eff}, and shear modulus G_{eff}, of FGMs can be given by

$$E_{eff} = (E_c - E_m)\left(\frac{z}{h} + \frac{1}{2}\right)^n + E_m,$$ (3a)

$$v_{eff} = (v_c - v_m)\left(\frac{z}{h} + \frac{1}{2}\right)^n + v_m,$$ (3b)

$$G_{eff} = (G_c - G_m)\left(\frac{z}{h} + \frac{1}{2}\right)^n + G_m.$$ (3c)

Using the above relation it is possible to obtain an insight into the variation of the material properties across the thickness of the beam for different power law indexes. Fig. 2a and b illustrates the variation of Young's modulus and Poisson's ratio of SUS304—Si_3N_4 FGM beam. The present study refers to Reddy and Chin [19] for material properties of various metals and ceramics.
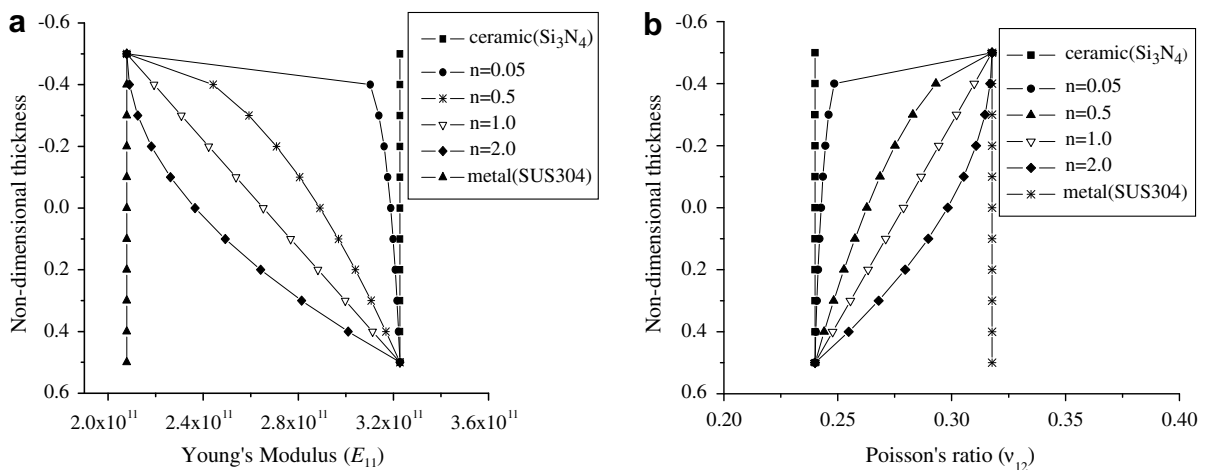

Fig. 2. Variation of Young's modulus and Poisson's ratio of SUS304–Si_3N_4 FGM beam along the thickness for various power law indexes.

2.2. Finite element formulation

The geometry of deformation for thick beams is shown in Fig. 3. The total rotation, $\frac{dw}{dx}$, can be expressed as the sum of bending rotation (or rotation of the normal) ψ_x and rotation due to shear γ. The displacement field based on the higher order theory as stated in Heyliger and Reddy [20] is written as

$$u(x,z) = u_0(x) + z\psi_x - \frac{4}{3h^2}z^3[\psi_x + w_{0,x}], \tag{4a}$$

$$w(x,z) = w_0(x), \tag{4b}$$

u_0 is the mid-plane axial displacement and w_0 is mid-plane transverse deflection. This displacement field is such that it accounts for traction free condition on the top and bottom surfaces of the beam. Several investigators have reported that using shear rotation instead of bending rotation improves the accuracy of the finite element analysis, for example, Chee et al. [21]. Therefore, the kinematics incorporating shear strain is as follows:

$$u(x,z) = u_0(x) - z(w_{0,x} - \gamma) - \frac{4}{3h^2}z^3\gamma, \tag{5a}$$

$$w(x,z) = w_0(x). \tag{5b}$$

The displacement fields described by Eqs. (4a), (4b) and (5a), (5b) are the basis for the stiffness matrix derivation.

2.3. Strain energy based on higher order theory in terms of rotation of normal, ψ_x

The normal strain, ε_{x1}, and the transverse shear strain, γ_{xz1}, based on the displacement field given by Eqs. (4a) and (4b) for one-dimension beam are as follows:

$$\varepsilon_{x1} = u_{,x} = u_{0,x} + z\psi_{x,x} - \alpha z^3[\psi_{x,x} + w_{0,xx}], \tag{6}$$

where $\alpha = \frac{4}{3h^2}$ and ε_{x1} is the axial normal strain. Subscript '1' stands for formulation based on rotation of normal as dof. Examining Eq. (6), it is essential to identify the following components of strains, namely, the membrane strain, ε_{m1}, bending strain, ε_{b1}, and strain due to higher order displacement, ε_{hs1} respectively. The transverse shear strain as per higher order displacement field is

$$\gamma_{xz1} = u_{,z} + w_{,x} = (1 - 3\alpha z^2)(\psi_x + w_{0,x}). \tag{7}$$
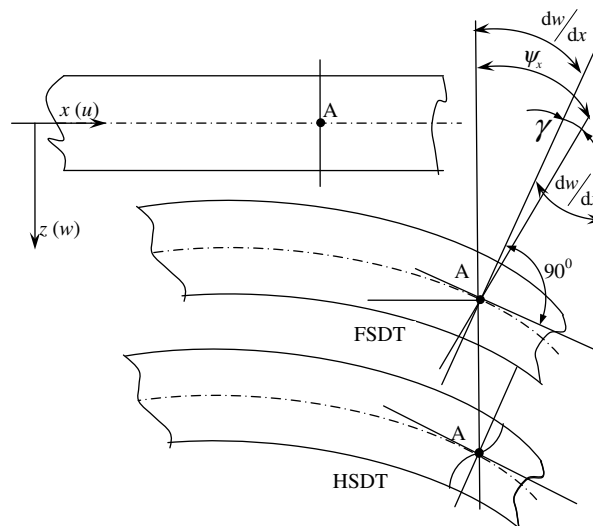

Fig. 3. Geometrical description of the deformation of thick beams.

Strain energy for a FGM beam with rotation of normal as a variable is given by the following expression:

$$U_1^e = \frac{b}{2} \int_0^l \int_z \left(\{ u_{0,x} + z\psi_{x,x} - \alpha z^3 (\psi_{x,x} + w_{0,xx}) \}^2 (Q_{xx})_{\text{eff}} + \{ (1 - 3\alpha z^2)(\psi_{x,x} + w_{0,xx}) \}^2 (Q_{xz})_{\text{eff}} \right) \mathrm{d}z \, \mathrm{d}x, \quad (8)$$

where $(Q_{xx})_{\text{eff}}$ is the effective longitudinal Young's modulus and $(Q_{xz})_{\text{eff}}$ is the effective transverse shear modulus. Based on the strain energy expression given by Eq. (8), the nodal degrees of freedom are, $(u_0 \quad w_0 \quad w_{0,x} \quad \psi_x)$. Evaluating the strain energy in Eq. (8) by substituting the strain components from Eqs. (6) and (7),

$$U_1^e = \frac{b}{2} \int_0^l \left(\varepsilon_{m1}^T A_{xx} \varepsilon_{m1} + \varepsilon_{b1}^T D_{xx} \varepsilon_{b1} + \varepsilon_{hs1}^T \alpha^2 H_{xx} \varepsilon_{hs1} + \gamma_{xz1}^T S_{xx} \gamma_{xz1} + 2\varepsilon_{m1}^T B_{xx} \varepsilon_{b1} - 2\varepsilon_{b1}^T \alpha F_{xx} \varepsilon_{hs1} - 2\varepsilon_{m1}^T \alpha E_{xx} \varepsilon_{hs1} \right) \mathrm{d}x,$$

$$(9)$$

where

$$(A_{xx}, B_{xx}, D_{xx}, E_{xx}, F_{xx}, H_{xx}) = \sum_{j=1}^{nlay} \int_{z_j}^{z_{j+1}} (1, z, z^2, z^3, z^4, z^6)(Q_{xx})_{\text{eff}} \, \mathrm{d}z, \quad (10a)$$

$$S_{xx} = \sum_{j=1}^{nlay} \int_{z_j}^{z_{j+1}} (1 - 3\alpha^2 z^2)(Q_{xz})_{\text{eff}} \mathrm{d}z. \quad (10b)$$

In the above expression the various coefficients are: A_{xx} is the extensional stiffness, B_{xx} bending–extension coupling stiffness, D_{xx} bending stiffness, E_{xx} warping–extension coupling stiffness, F_{xx} warping–bending coupling stiffness, H_{xx} warping–higher order bending coupling stiffness, S_{xx} shear stiffness. The quantities, $(Q_{xx})_{\text{eff}}$ and $(Q_{xz})_{\text{eff}}$, for FGM beams will be evaluated using Eqs. (3a) and (3c) as follows:

$$(Q_{xx})_{\text{eff}} = \frac{E_{\text{eff}}}{1 - v_{\text{eff}}^2} \quad \text{and} \quad (11a)$$

$$(Q_{xz})_{\text{eff}} = \frac{E_{\text{eff}}}{2(1 + v_{\text{eff}})}. \quad (11b)$$

2.4. Strain energy based on higher order theory in terms of shear rotation, γ

The normal strain in terms of shear rotation will be

$$\varepsilon_{x2} = u_{,x} = u_{0,x} - z(w_{0,xx} - \gamma_{,x}) - \alpha z^3 \gamma_{,x}. \quad (12)$$

Subscript '2' stands for formulation is based on shear rotation as the variable. The transverse shear strain will be expressed in terms of shear rotation as follows:

$$\gamma_{xz2} = u_{,z} + w_{,x} = \gamma(1 - 3\alpha z^2). \quad (13)$$

The strain energy in terms of shear rotation will be,

$$U_2^e = \frac{b}{2} \int_0^l \int_z \left(\{ u_{0,x} - z(w_{0,xx} - \gamma_{,x}) - \alpha z^3 \gamma_{,x} \}^2 (Q_{xx})_{\text{eff}} + \{ (1 - 3\alpha z^2)\gamma \}^2 (Q_{xz})_{\text{eff}} \right) \mathrm{d}z \, \mathrm{d}x. \quad (14)$$

Strain energy in terms of strain components and integrated reduced stiffness coefficients is as follows:

$$U_2^e = \frac{b}{2} \int_0^l \left(\varepsilon_{m2}^T A_{xx} \varepsilon_{m2} + \varepsilon_{b2}^T D_{xx} \varepsilon_{b2} + \varepsilon_{hs2}^T \alpha^2 H_{xx} \varepsilon_{hs2} + \gamma_{s2}^T S_{xx} \gamma_{s2} - 2\varepsilon_{m2}^T B_{xx} \varepsilon_{b2} - 2\varepsilon_{m2}^T \alpha E_{xx} \varepsilon_{hs2} + 2\varepsilon_{b2}^T \alpha F_{xx} \varepsilon_{hs2} \right) \mathrm{d}x.$$

$$(15)$$

The nodal degrees of freedom for the finite element will be, $\mathbf{q}_{2e} = \{ u_{0i} \quad w_{0i} \quad w_{0i,x} \quad \gamma_i \}^T$, where $i = 1, 2$.

2.5. Stiffness matrix and load vector

The principle of minimum potential energy for an elastic body is followed to derive the finite element matrices. Considering the work done by internal forces and the work done by the transverse load intensity, the total potential energy is

$$\Pi = \frac{1}{2} \int_V \boldsymbol{\sigma}^{\mathrm{T}} \boldsymbol{\varepsilon} \, \mathrm{d}V - \int_S \mathbf{d}^{\mathrm{T}} \mathbf{f} \, \mathrm{d}S, \tag{16}$$

where $\mathbf{f}$ = distributed forces per unit area, and $\mathbf{d}$ = displacement vector, $\{u_0 \ w_0 \ \psi_{x0}\}^{\mathrm{T}}$ or $\{u_0 \ w_0 \ \gamma\}^{\mathrm{T}}$. Linear interpolation functions, N_{L}, are chosen for axial displacement, rotation of the normal and shear rotation. Hermite cubic interpolation functions, N_{H}, are chosen for transverse deflection and slope. The strain energy expression, Eq. (9), in terms of strain displacement matrix and element degrees of freedom is

$$U_1^{\mathrm{e}} = \frac{b}{2} \mathbf{q}_{1e}^{\mathrm{T}} \int_0^l \left\{ \mathbf{B}_{\mathrm{m1}}^{\mathrm{T}} A_{xx} \mathbf{B}_{\mathrm{m1}} + \mathbf{B}_{\mathrm{b1}}^{\mathrm{T}} D_{xx} \mathbf{B}_{\mathrm{b1}} + \mathbf{B}_{\mathrm{hs1}}^{\mathrm{T}} \alpha^2 H_{xx} \mathbf{B}_{\mathrm{hs1}} + \left(\mathbf{B}_{\mathrm{m1}}^{\mathrm{T}} B_{xx} \mathbf{B}_{\mathrm{b1}} + \mathbf{B}_{\mathrm{b1}}^{\mathrm{T}} B_{xx} \mathbf{B}_{\mathrm{m1}} \right) \right.$$
$$\left. - \left(\mathbf{B}_{\mathrm{b1}}^{\mathrm{T}} \alpha F_{xx} \mathbf{B}_{\mathrm{hs1}} + \mathbf{B}_{\mathrm{hs1}}^{\mathrm{T}} \alpha F_{xx} \mathbf{B}_{\mathrm{b1}} \right) - \left(\mathbf{B}_{\mathrm{m1}}^{\mathrm{T}} \alpha E_{xx} \mathbf{B}_{\mathrm{hs1}} + \mathbf{B}_{\mathrm{b1}}^{\mathrm{T}} \alpha E_{xx} \mathbf{B}_{\mathrm{m1}} \right) + \mathbf{B}_{\mathrm{s1}}^{\mathrm{T}} S_{xx} \mathbf{B}_{\mathrm{s1}} \right\} \mathrm{d}x \, \mathbf{q}_{1e}. \tag{17}$$

Using the principle of stationary potential energy, the first variation of Π, i.e. $\delta\Pi = 0$, leads to different finite element matrices and are described below. The stiffness matrix containing the rotation of the normal is

$$(\mathbf{K}^{\mathrm{e}})_1 = (\mathbf{K}_{\mathrm{m}})_1 + (\mathbf{K}_{\mathrm{b}})_1 + (\mathbf{K}_{\mathrm{hs}})_1 + (\mathbf{K}_{\mathrm{c1}})_1 - (\mathbf{K}_{\mathrm{c2}})_1 - (\mathbf{K}_{\mathrm{c3}})_1 + (\mathbf{K}_{\mathrm{s}})_1. \tag{18}$$

Different components of the overall stiffness matrix are, $(\mathbf{K}_{\mathrm{m}})_1$ the membrane stiffness matrix, $(\mathbf{K}_{\mathrm{b}})_1$ the bending stiffness matrix, $(\mathbf{K}_{\mathrm{hs}})_1$ the stiffness matrix due to higher order displacement term, $(\mathbf{K}_{\mathrm{s}})_1$ the transverse shear stiffness matrix (involving the effect of rotation of the normal), and $(\mathbf{K}_{\mathrm{c1}})_1$, $(\mathbf{K}_{\mathrm{c2}})_1$ and $(\mathbf{K}_{\mathrm{c3}})_1$ are the coupling matrices due to coupling between membrane, bending, and higher order displacement.

$$(\mathbf{K}_{\mathrm{m}})_1 = \int_0^l \mathbf{B}_{\mathrm{m1}}^{\mathrm{T}} A_{xx} \mathbf{B}_{\mathrm{m1}} \mathrm{d}x, \quad (\mathbf{K}_{\mathrm{b}})_1 = \int_0^l \mathbf{B}_{\mathrm{b1}}^{\mathrm{T}} D_{xx} \mathbf{B}_{\mathrm{b1}} \mathrm{d}x,$$

$$(\mathbf{K}_{\mathrm{hs}})_1 = \int_0^l \mathbf{B}_{\mathrm{hs1}}^{\mathrm{T}} \alpha^2 H_{xx} \mathbf{B}_{\mathrm{hs1}} \mathrm{d}x, \quad (\mathbf{K}_{\mathrm{s}})_1 = \int_0^l \mathbf{B}_{\mathrm{s1}}^{\mathrm{T}} S_{xx} \mathbf{B}_{\mathrm{s1}} \mathrm{d}x,$$

$$(\mathbf{K}_{\mathrm{c1}})_1 = \int_0^l \left(\mathbf{B}_{\mathrm{m1}}^{\mathrm{T}} B_{xx} \mathbf{B}_{\mathrm{b1}} + \mathbf{B}_{\mathrm{b1}}^{\mathrm{T}} B_{xx} \mathbf{B}_{\mathrm{m1}} \right) \mathrm{d}x, \quad (\mathbf{K}_{\mathrm{c2}})_1 = \int_0^l \left(\mathbf{B}_{\mathrm{b1}}^{\mathrm{T}} \alpha F_{xx} \mathbf{B}_{\mathrm{hs1}} + \mathbf{B}_{\mathrm{hs1}}^{\mathrm{T}} \alpha F_{xx} \mathbf{B}_{\mathrm{b1}} \right) \mathrm{d}x,$$

$$(\mathbf{K}_{\mathrm{c3}})_1 = \int_0^l \left(\mathbf{B}_{\mathrm{m1}}^{\mathrm{T}} \alpha E_{xx} \mathbf{B}_{\mathrm{hs1}} + \mathbf{B}_{\mathrm{hs1}}^{\mathrm{T}} \alpha E_{xx} \mathbf{B}_{\mathrm{m1}} \right) \mathrm{d}x.$$

Considering the uniform load intensity, $\mathbf{f}$, in the transverse direction, the nodal load vector, p_{UDL}^e, is given by

$$p_{\mathrm{UDL}}^{\mathrm{e}} = \left\{ 0 \quad \frac{\mathbf{f}l}{2} \quad \frac{\mathbf{f}l^2}{12} \quad 0 \quad 0 \quad \frac{\mathbf{f}l}{2} \quad \frac{-\mathbf{f}l^2}{12} \quad 0 \right\}^{\mathrm{T}}. \tag{19}$$

Similarly, using the strain energy expression containing the shear rotation term, Eq. (15), it is possible to arrive at the second stiffness matrix. The nodal variables like, axial displacement and shear rotation are evaluated using linear interpolation function and Hermite cubic interpolation functions are chosen for evaluation of the variation transverse deflection and slope along the element. Applying the principle of stationary potential energy, the stiffness matrix containing the shear rotation term can be obtained as follows:

$$(\mathbf{K}^{\mathrm{e}})_2 = (\mathbf{K}_{\mathrm{m}})_2 + (\mathbf{K}_{\mathrm{b}})_2 + (\mathbf{K}_{\mathrm{hs}})_2 + (\mathbf{K}_{\mathrm{s}})_2 - (\mathbf{K}_{\mathrm{c1}})_2 - (\mathbf{K}_{\mathrm{c2}})_2 + (\mathbf{K}_{\mathrm{c3}})_2. \tag{20}$$

The various stiffness matrices in Eq. (20) have the same meaning as described for Eq. (18). However, the differences arise in the transverse shear stiffness matrix $(\mathbf{K}_{\mathrm{s}})_2$, and coupling matrices due to Eq. (13). Based on the formulation discussed, FORTRAN codes are developed and will be referred to as: (i) FGM-HSDT-RN (higher order theory with rotation of normal as one of the dof) and (ii) FGM-HSDT-SR (higher order theory with shear rotation as dof).

3. Numerical results and discussion

Numerical exercises are carried out to analyze static deflection characteristics and stress variation in various FGM beams like SUS304–Si$_3$N$_4$, SUS304–Al$_2$O$_3$, SUS304–ZrO$_2$, Ti–6Al–4V–Si$_3$N$_4$, Ti–6Al–4V–Al$_2$O$_3$, and Ti–6Al–4V—ZrO$_2$. A moderately thick FGM beams with $L/h = 15$ and length equal to 1.2 m is considered for the study. The influence of metal–ceramic constituents is examined by varying the power law exponent. Boundary conditions for the beams are clamped–clamped and simply supported. Width of the beam is unity. The beam is divided into number of layers in thickness direction and each layer is assumed to be isotropic. Eqs. (1a) and (1b) in conjunction with Eq. (2) are used to evaluate the effective properties of each layer and hence the integrated stiffness coefficients, Eqs. (10a) and (10b). For deflection analysis properties are evaluated at the mid of each layer whereas for stress analysis properties are evaluated at top of each layer. To obtain a proper representation of the constitutive matrix for FGM beam, a convergence study is required for the choice on the number of layer across the thickness. It is found that a convergence of the elastic constants is achieved with 70 layers across the thickness.

3.1. Convergence study

Table 1 gives the convergence study for FGM-HSDT-RN and FGM-HSDT-SR. FGM beam of SUS304-Si$_3$N$_4$ with clamped free boundary condition, $L/h = 15$ and power law exponent of 1000 (metal rich) is taken up for the study. The non-dimensional deflection is given by the relation: $\overline{\overline{w}} = \frac{w \times E_{11} \times h^3 \times b}{F \times L^3}$, where w is the transverse deflection in meters, E_{11} is Young's modulus in material direction '1' and F is the applied point load. Convergence is achieved with 20 elements using the code FGM-HSDT-SR whereas for FGM-HSDT-RN convergence is obtained for 30 elements. Thus it can be seen that relatively faster convergence is obtained for HSDT-FGM-SR when compared to FGM-HSDT-RN. All the results given here after will correspond to beam with 30 finite elements.

3.2. Validation

A systematic and thorough validation of the FGM-HDST-RN and FGM-HDST-SR FORTRAN codes are carried out. From Table 2 it can be observed that FGM-HSDT-SR gives same results for thin beam as reported by Shi et al. [3]. The non-dimensional deflection are given by, $\overline{w} = \frac{wD_{xx}}{FL^3}$. The results presented in Table 3 uses beam idealized with eight finite elements for clamped–clamped (CC), clamped–free (CF) and simply supported (SS), and 10 finite elements for clamped–simply supported (CS). For thick beams and various boundary conditions the results from the present code differ marginally when compared to those reported

Table 1
Convergence study on finite elements for FGM beams

Number of elements	$\overline{\overline{w}}$	
	FGM-HSDT-SR	FGM-HSDT-RN
2	3.602	3.384
5	3.604	3.573
20	3.605	3.604
30	3.605	3.605

Table 2
Non-dimensional tip deflections of isotropic cantilevered beam using one finite element for the beam

Formulation (or computer code)	Aspect ratio		
	5	10	1000
HQCB-8A, Ref. [3]	0.3451	0.3363	0.3333
FGM-HSDT-SR	0.3419	0.3354	0.3333

Table 3
Deflection validation for cross ply beams with different boundary conditions

Boundary conditions	$L/h = 15$		
	HQCB-8a, Ref. [3]	FGM-HSDT-SR	% Error
CC	0.03344	0.029929	10.49
CF	1.0038	0.9108	9.2
CS	0.05657	0.0517	8.6
SS	0.1112	0.1035	6.9

by Shi et al. [3]. The difference in the results can be accounted from the fact that Shi et al. uses a quasi-conforming technique wherein the element strain field is interpolated directly over the element domain rather than differentiated from the assumed displacement field. Also it is to be mentioned that there was less faster convergence when compared to the element proposed by Shi et al. Deflection results of Table 4 were also in exact agreement for simply supported isotropic beam provided the number of elements idealized for the beam is two times for the present code (FGM-HSDT-RN) when compared to Heyliger and Reddy [20].

A cantilever beam is loaded in the axial direction with a unit load and stresses are obtained at the tip. The shear stress is zero while the axial stress is 20 N/m^2 which is in agreement with that obtained by Chakraborty et al. [4]. The depth wise distribution of stress is shown in Fig. 4. Geometric dimension of the beam are $L = 0.5$ m, $h = 0.05$ m, load = 1.0 N at the tip and power law index ($n = 400$ (metal)). The material properties are: (i) steel: $E = 210$ GPa, $G = 80$ GPa, $\alpha = 14.0 \times 10^{-6}$ °C^{-1}; (ii) Alumina: $E = 390$ GPa, $G = 137$ GPa, $\alpha = 6.9 \times 10^{-6}$ °C^{-1}. We also attempt to validate for the example of orthotropic functionally graded cantilever

Table 4
Comparison of deflection for cantilever beam with Ref. [20]

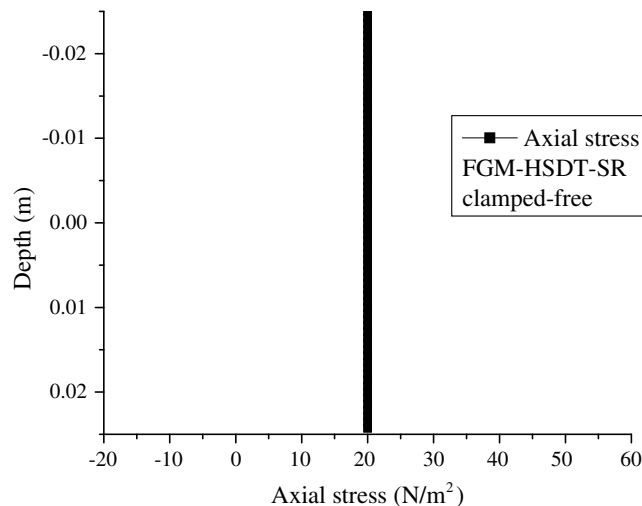| L	h					
160	12	Number of elements	2	4	8	16
		Ref. [20]	30.838	32.368	32.742	32.823
		FGM-HSDT-RN	30.838	32.367	32.742	32.822
80	12	Ref. [20]	3.9234	4.1105	4.1506	4.1567
		FGM-HSDT-RN	3.9233	4.1104	4.1505	4.1567
12	12	Ref. [20]	0.023551	0.023741	0.023874	0.023931
		FGM-HSDT-RN	0.023551	0.023741	0.023874	0.0239307

Fig. 4. Depth wise axial stress distribution in steel–alumina clamped–free FGM beam under unit axial load.

beam subjected to uniform pressure on its upper surface, from Zhong and Yu [11]. The dimensions of the beam are length $L = 1.0$ m, thickness $h = 0.2$ m. The grading function is of the type $F(z) = e^{\frac{\alpha z}{h}}$, where α is the grading index. The material properties of the beam at $z = z_0$ are

$$\begin{bmatrix} s_{11} & s_{13} & 0 \\ s_{31} & s_{33} & 0 \\ 0 & 0 & s_{44} \end{bmatrix} = 10^{-12} \begin{bmatrix} 5.41 & -1.51 & 0 \\ -1.51 & 95.2 & 0 \\ 0 & 0 & 137.0 \end{bmatrix} \text{Pa}^{-1}.$$

It can be noticed from Fig. 5 that there is certainly good agreement with the analytical solution of Zhong and Yu.

3.3. Studies on displacement field variables for various FGM beams

Transverse deflection characteristics for various FGM beams with clamped–clamped and simply supported boundary conditions were examined. The non-dimensional deflection are given by the relation: $\underline{w} = \frac{wbE_{\text{metal}}h^3}{\mathbf{f}L^4} \times 100$, where E_{metal} is Young's modulus of metal considered. From Fig. 6a and b it can be observed that, deflection of metal rich composition is more when compared to ceramic rich SUS304–Si$_3$N$_4$ FGM beam. This can be accounted for the Young's modulus of ceramic (Si$_3$N$_4$; 322.76 GPa) being high when compared to that of metal (SUS304; 207.89 GPa). This is further clear by referring to Fig. 2a indicating the variation of Young's modulus with different power law exponent for SUS304–Si$_3$N$_4$ FGM beam. Hence for SUS304–Si$_3$N$_4$ FGM beam, transverse deflection decreases as power law exponent is decreased. From Fig. 7a and b, the deflections for metal rich SUS304–ZrO$_2$ beam are less than that of ceramic rich beam. This is contrary to that observed in Fig. 6a and b. This is because the Young's modulus for ceramic (ZrO$_2$; 168.06 GPa) is less than that of metal (SUS304). Comparing the deflections of FGM SUS304–Si$_3$N$_4$ and SUS304–ZrO$_2$, it is found that irrespective of the power law index and boundary condition, FGM beam of SUS304–Si$_3$N$_4$ provides better resistance to load. Similar conclusions were arrived at for FGM beam constituting Ti–6Al–4V with two different ceramic, Si$_3$N$_4$ and ZrO$_2$. The effect on the deflection pattern as a result of interchanging the loading from metal rich face to ceramic rich face is studied. The non-dimensional maximum deflection of clamped–clamped SUS304–Si$_3$N$_4$ FGM beam is given in Table 5. $\underline{w}$ is the non-dimensional deflection when loading is applied to metal rich face which is being on the top. $\underline{w}_{\text{CT}}$ is the non-dimensional deflection when loading is applied to ceramic rich face which is on the top. To simulate results with loading on metal rich surface, Eqs. (1a) and (1b) hold true i.e., metal is always at the top and ceramic content will be more towards the
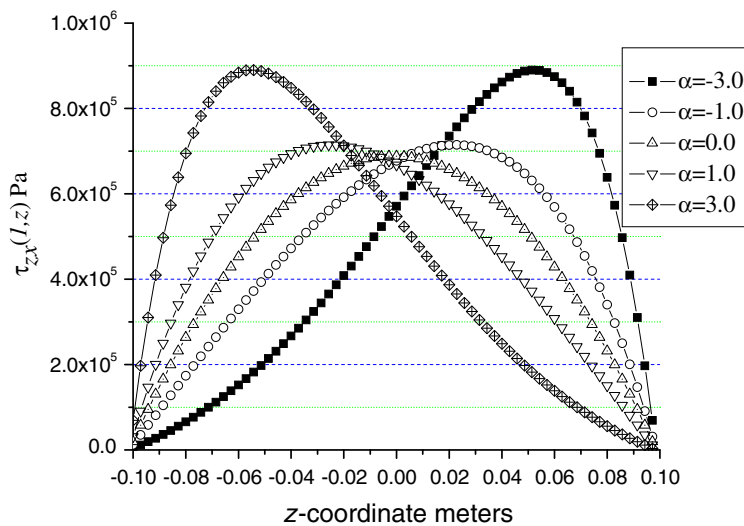

Fig. 5. Transverse shear stress at the clamped end of clamped free beam with grading index as $F(z) = e^{\frac{\alpha z}{h}}$ obtained from finite element solution based on higher order theory (FGM-HSDT-SR code).
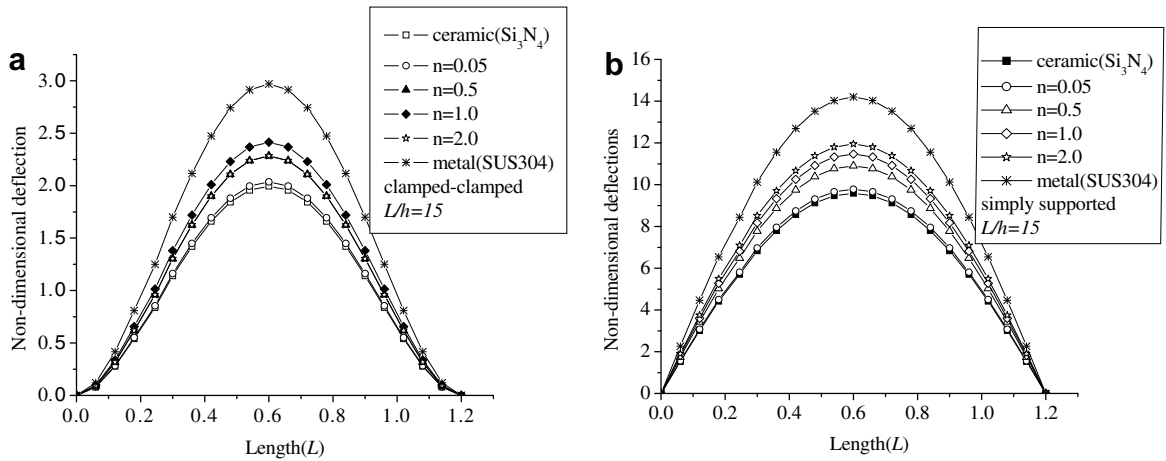
Fig. 6. Non-dimensional deflection of SUS304–Si$_3$N$_4$ beam along length under UDL.
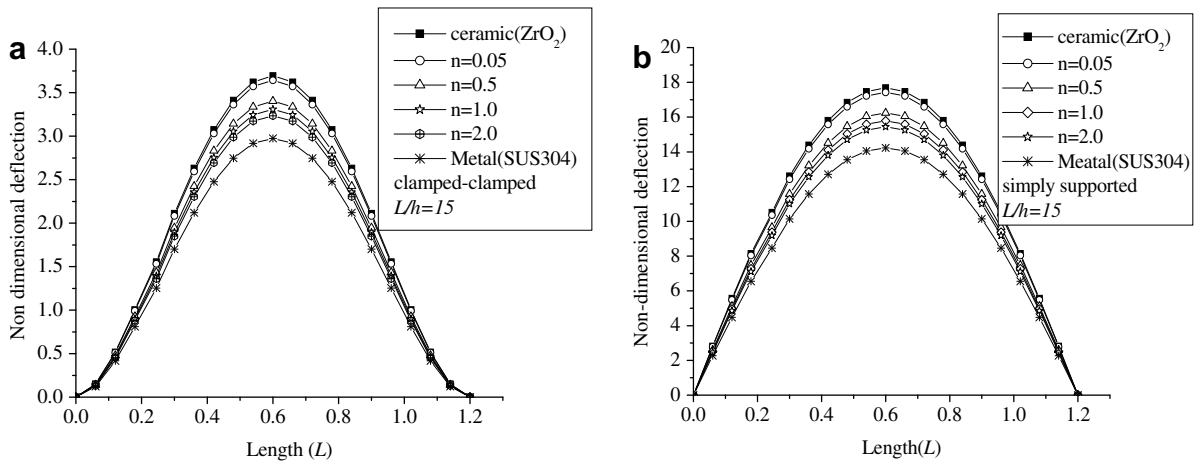

Fig. 7. Non-dimensional deflection of SUS304–ZrO$_2$ beam along length under UDL.

Table 5
Non-dimensional maximum deflection of clamped–clamped SUS304–Si$_3$N$_4$ FGM beam of $L/h = 15$

n	$\underline{w}$ (loading on metal rich face)	$\underline{w}_{CT}$ (loading on ceramic rich face)
0.0	1.998	2.976
0.05	2.0378	2.890
0.5	2.285	2.5419
1.0	2.417	2.417
2.0	2.5282	2.317
400.0	2.9733	1.999

bottom of the beam. When ceramic is required on the top of the beam and metal at the bottom the following relations are used:

$$V_m = \left(\frac{z}{h} + \frac{1}{2}\right)^n \quad \text{and} \tag{21a}$$

$$V_c = 1 - V_m. \tag{21b}$$

From Table 5 it can be observed that for homogeneous beam of ceramic and metal and for linear variation i.e. $n = 1$, deflections remain same even if the loading faces are interchanged. But for power law index other than 0.0, 1.0, and 400 the deflection does not remain the same. This is because effective material property changes. For example, for $n = 0.5$, $\underline{w}$ is less than $\underline{w}_{CT}$. Table 6 shows similar study for SUS304–ZrO$_2$ FGM beam.

3.4. Comparison of deflection evaluated based on FSDT and HSDT

A FORTRAN computer code has also been developed based on first-order shear deformation theory, following the formulation discussed in Mathew et al. [22]. The features of this finite element are: (i) six dof per node namely axial displacement, transverse deflection, rotation of the normal and their derivative with respect to beam axis, and (ii) Hermite interpolation functions are used to evaluate the displacement field within the element. (iii) Beam when idealized with 90 elements provides a converged solution. Table 7 lists the non-dimensional transverse deflection, $\overline{\overline{w}}$, with point load acting at the tip of a SUS304–Si$_3$N$_4$ cantilever FGM beam obtained from various theories and for varying L/h ratios. Power law exponent used is 400 (i.e. metal rich beam). The deflection for FGM beams with different power law index evaluated by the FSDT and two HSDT are listed in Table 8. From Tables 7 and 8 it can be seen that both the shear deformation theories yields deflections with negligible difference. But FGM-FSDT needs 90 finite elements whereas higher order theories produce results with 30 elements. If one is interested to study the shear stress variation across the thickness higher order theory would be more useful.

Table 6
Non-dimensional maximum deflection of clamped–clamped SUS304–ZrO$_2$ FGM beam of $L/h = 15$

n	$\underline{w}$ (loading on metal rich face)	$\underline{w}_{CT}$ (loading on ceramic rich face)
0.0	3.697	2.976
0.05	3.645	3.013
0.5	3.405	3.216
1.0	3.311	3.311
2.0	3.237	3.389
400.0	2.978	3.695

Table 7
Non-dimensional tip deflection vs. L/h for SUS304–Si$_3$N$_4$ cantilever beam

L/h	Non-dimensional deflection $\overline{\overline{w}}$		
	FGM-FSDT	FGM-HSDT-RN	FGM-HSDT-SR
5	3.704	3.714	3.714
10	3.608	3.622	3.622
15	3.591	3.604	3.605
30	3.581	3.593	3.595
60	3.577	3.589	3.591
100	3.577	3.589	3.591

Table 8
Non-dimensional tip deflection vs. power law index for SUS304–Si$_3$N$_4$ cantilever beam, $L/h = 15$

n	Non-dimensional deflection $\overline{\overline{w}}$		
	FGM-FSDT	FGM-HSDT-RN	FGM-HSDT-SR
Ceramic	2.426	2.436	2.436
0.05	2.475	2.484	2.484
0.5	2.775	2.785	2.786
1.0	2.930	2.942	2.942
2.0	3.054	3.067	3.067
Metal	3.591	3.605	3.605

3.5. Stresses in titanium alloy–ceramics and SUS304–ceramics FGM beams

The axial (bending or longitudinal) stresses and transverse shear stresses in various metal–ceramic FGM beams are evaluated using FGM-HSDT-SR and their discussion is considered now. The stresses are evaluated at the centre of each finite element and the results presented correspond to 15th element. The stresses are non-dimensionalized using the relation, $(\overline{\sigma}_{xx}, \overline{\tau}_{xz}) = \frac{(\sigma_{xx}, \tau_{xz})h^2}{\mathbf{f}L^2}$, where, σ_{xx}, τ_{xz}, are the axial and transverse shear stress and $\mathbf{f}$ is the uniformly distributed load. The stresses are evaluated for loading cases involving load on metal rich face and load on ceramic rich face and hence the effect on stress distribution is investigated thoroughly.

Fig. 8 illustrates the axial stress plot for Ti–6Al-4V–ZrO_2 FGM beam with clamped–clamped edges and UDL on the metal rich face. As expected the axial stresses are compressive on the metal rich face (top) and tensile on the ceramic rich face (bottom). Note that the plots read negative sign for tensile stresses and positive sign for compressive stresses. The variation of axial stress across the thickness is linear for homogeneous constituent FGM. From Fig. 8, it is to be noted that, for FGM with $n = 400$, which is suppose to be metal rich, there is a kink in the stress variation close to bottom surface. This is because, in spite of choosing high n, it is not possible to represent the beam fully with metal and some fraction of ceramic exists at the bottom face. The axial stress variation is not linear for FGM beam with power law index: 0.05, 0.5, 1.0, 2.0. FGM beam with $n = 2.0$, the tensile stresses at the bottom is maximum. The bottom of FGM beam has ceramic constituent where the stresses are maximum. Further, the neutral plane shifts depending on the power law index. For homogeneous FGM beams, i.e. for $n = 0$ and 400, the neutral plane exist through the mid of the thickness. This is not true for power law index $n = 0.05, 0.5, 1.0, 2.0$, wherein the neutral plane shifts towards the bottom face (ceramic rich face). The shift in the neutral plane is predominant for $n = 1.0$ and 2.0. This shift in the neutral plane is expected because of effective material properties change across the thickness. The magnitude of the compressive and tensile axial stresses at the top fibre and bottom fibre respectively are unequal in magnitude for FGM beams with power law indexes 0.05, 0.5, 1.0, and 2.0. Further, the tensile axial stresses are higher in magnitude when compared to compressive axial stresses. The plot of shear stress across the FGM beam of Ti–6Al–4V–ZrO_2 is presented in Fig. 9. The loading is directed on the metal rich face. It is observed form the figure that, the shear stress across beam thickness is symmetric about the neutral plane, however, the relative location of the neutral plane is not the same for FGM beams with different power law indexes considered in the study. The comment on the location of the neutral plane has been the outcome based on the shear stress plots. For power law index other than homogeneous composition, neutral plane shifts towards the ceramic rich face.

Fig. 10 demonstrates the variation of axial stress across the FGM beams of Ti–6Al–4V–ZrO_2 with clamped–clamped boundary condition and the loading is brought on to the ceramic rich face. Comparing
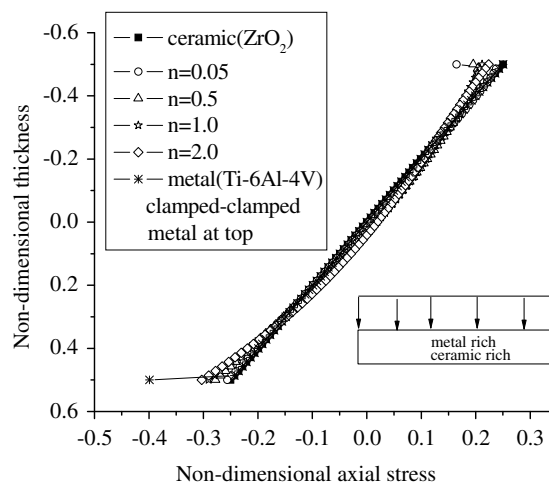

Fig. 8. Non-dimensional axial stresses in clamped–clamped Ti–6Al–4V–ZrO_2 FGM beam across the thickness.
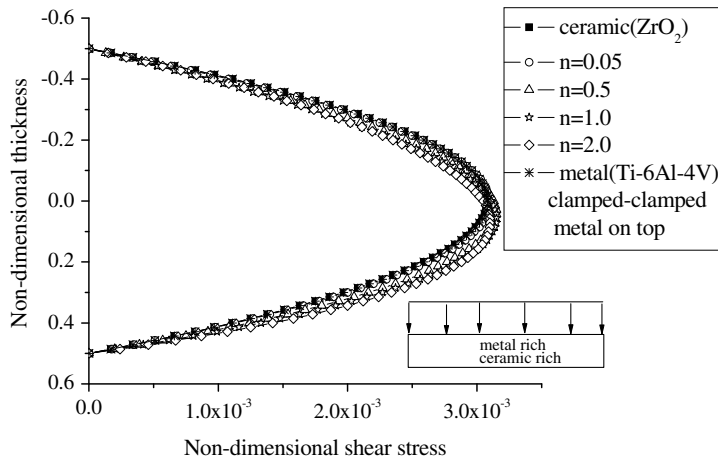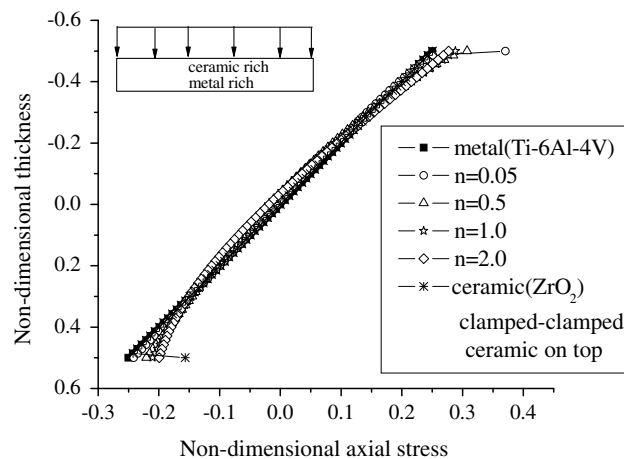
Fig. 9. Non-dimensional transverse shear stresses in clamped–clamped Ti–6Al–4V–ZrO$_2$ FGM beam across the thickness.

Fig. 10 with Fig. 8, it is seen that the stress profile through the thickness is not the same, hence the effect of interchanging the loading face. The axial stress variation is linear for $n = 0$ and 400. For power law index $n = 0.05, 0.5, 1.0$ and 2.0, the axial stress variation across the thickness is not linear. The tensile stress is minimum for $n = 2.0$, since the constituent is more of metal, which provides better resistance to load. The neutral plane is same for homogeneous FGM beams, i.e., at half the thickness, but for FGM with power law indexes 0.05, 0.5, 1.0 and 2.0, the neutral plane shifts towards the top (i.e. ceramic rich face). In Fig. 10, it is noticed that the compressive axial stress are high in magnitude at the top when compared to the axial tensile stress at the bottom for FGM beams with power law indexes other than 0.0 and 400.0.

The plots of transverse shear stress for Ti–6Al–4V–ZrO$_2$ beam with clamped–clamped boundary condition and loading put on ceramic rich face is shown in Fig. 11. Comparing Fig. 11 with Fig. 9, it is seen that the neutral plane shifts upwards towards the ceramic rich face. Thus it is to be noted that the neutral plane is close to ceramic rich face irrespective of the load is borne by metal or ceramic rich face. Similar studies on the stress distributions were conducted for simply supported Ti–6Al–4V–ZrO$_2$ FGM beam under similar conditions mentioned for clamped–clamped FGM beam and only one stress plot is presented as in Fig. 12. The magnitude of axial stress is high for simply supported beam when compared to clamped–clamped beam.

Plots of axial stresses for FGM Ti–6Al–4V–Al$_2$O$_3$, and SUS304–Al$_2$O$_3$ are presented in Figs. 13, 15 and 17. Transverse shear stresses for FGM Ti–6Al–4V–Al$_2$O$_3$, and SUS304–Al$_2$O$_3$ can be studied through Figs. 14, 16

Fig. 10. Non-dimensional axial stresses in clamped–clamped Ti–6Al–4V–ZrO$_2$ FGM beam across the thickness.
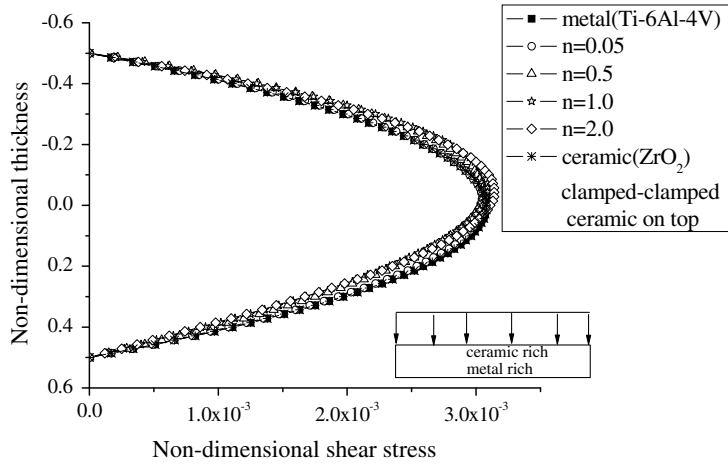
Fig. 11. Non-dimensional transverse shear stresses in clamped–clamped Ti–6Al–4V–ZrO₂ FGM beam across the thickness.
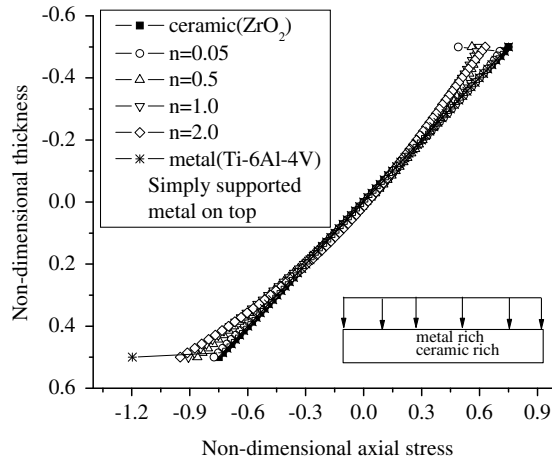

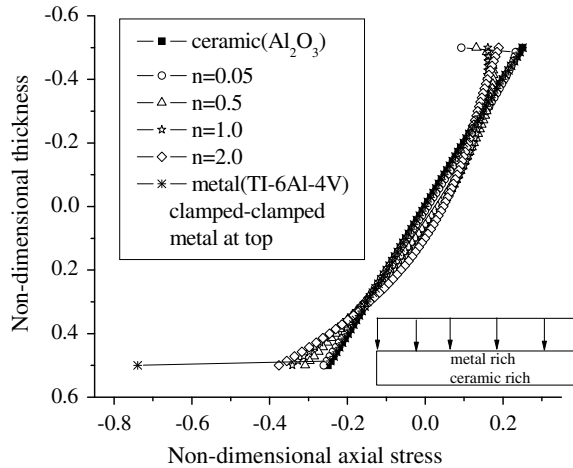Fig. 12. Non-dimensional axial stresses in simply supported Ti–6Al–4V–ZrO₂ FGM beam across the thickness.

Fig. 13. Non-dimensional axial stresses in clamped–clamped Ti–6Al–4V–Al₂O₃ FGM beam across the thickness.
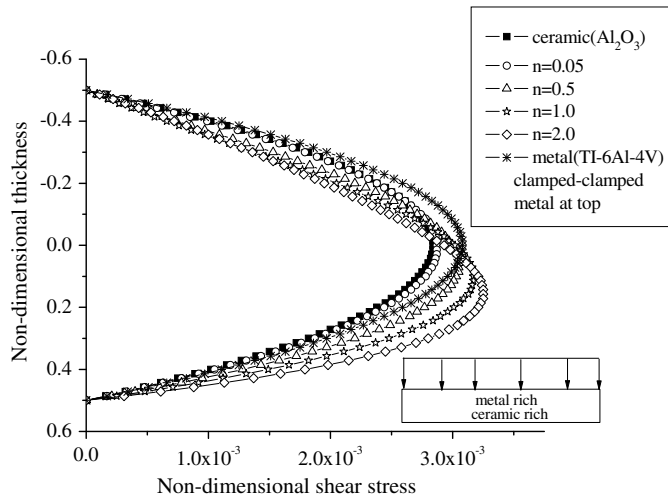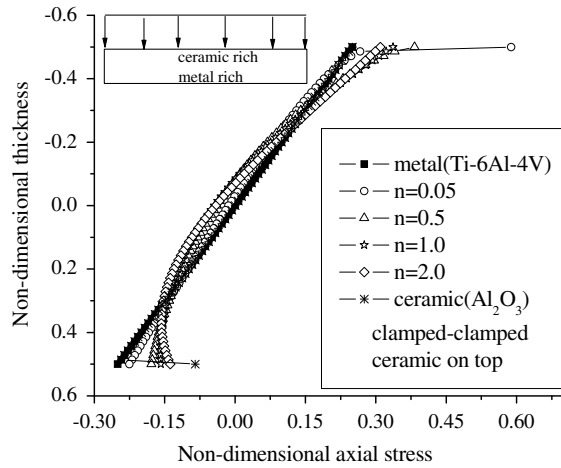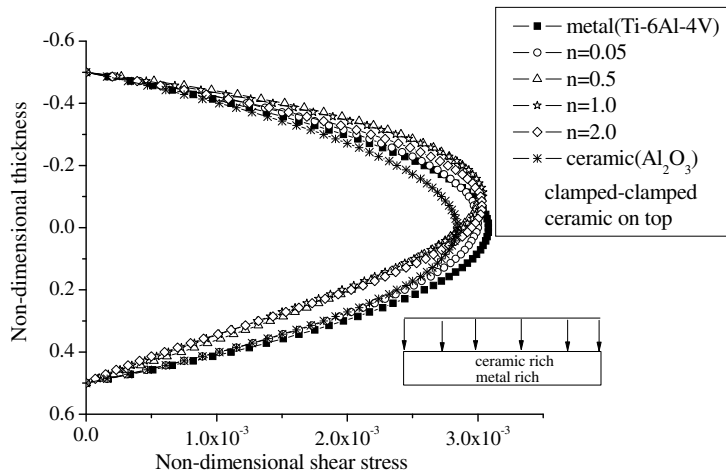
Fig. 14. Non-dimensional transverse shear stresses in clamped–clamped Ti–6Al–4V–Al₂O₃ FGM beam across the thickness.

Fig. 15. Non-dimensional axial stresses in clamped–clamped Ti–6Al–4V–Al₂O₃ FGM beam across the thickness.

Fig. 16. Non-dimensional transverse shear stresses in clamped–clamped Ti–6Al–4V–Al₂O₃ FGM beam across the thickness.
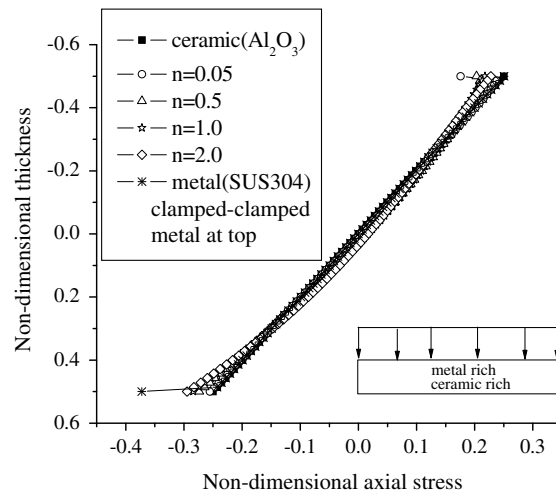
Fig. 17. Non-dimensional axial stresses in clamped–clamped SUS304–Al$_2$O$_3$ FGM beam across the thickness.
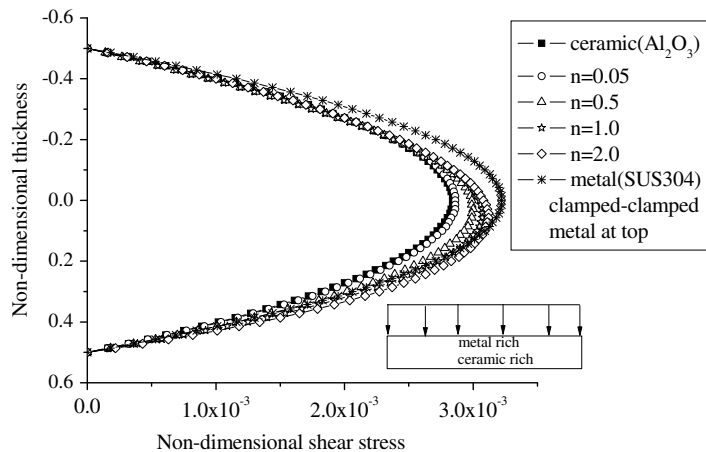

Fig. 18. Non-dimensional transverse shear stresses in clamped–clamped SUS304–Al$_2$O$_3$ FGM beam across the thickness.

and 18. A thorough examination of these results reveal that the profile of the axial stress distribution depends on the power law index $n = 0.05, 0.5, 1.0$ and 2.0 and also the load bearing surface. The magnitude of the maximum tensile stress and compressive stress are highly dependent on the metal–ceramic combinations, load bearing surface being either metal or ceramic and finally the power law index.

Finally, depending on the metal ceramic combination, the transverse shear stresses may differ considerably for varying values of power law index. This can be observed for FGM beam Ti–6Al–4V–Al$_2$O$_3$ (Figs. 14 and 16) and SUS304–Al$_2$O$_3$ (Fig. 18) where the shear stress profile are prominently separated from one another depending on the value of power law index, n, whereas for Ti–6Al–4V–ZrO$_2$, the shear stress (Figs. 9 and 11) profiles are close to one another irrespective of the value of n. This nature of closeness of shear stress profiles may be due to large difference in the Young's modulus of metal–ceramic in Ti–6Al–4V–Al$_2$O$_3$ (105.69 GPa and 320.7 GPa respectively).

4. Conclusions

Higher order beam theory was effectively used to study extensively the static displacement field components, axial stress and shear stress distribution in various FGM beams. For FGM beams of SUS304–

Si_3N_4, Ti–6Al–4V–Si_3N_4 and Ti–6Al–4V–ZrO_2, it was observed that the deflections for a given boundary condition are more for metal rich beam when compared to ceramic rich beam and deflection increases as the power law index increases. For SUS304–ZrO_2 the reverse was true. The axial stress distribution through the depth is linear for metal–ceramic FGMs when power law index value leads to a homogeneous beam. For power law index other than homogeneous composition the stress profile is not linear. The magnitude of maximum axial tensile stress and maximum axial compressive stress is dependent on the metal–ceramic combination as well as load bearing surface. When the load is changed from metal face to ceramic face, the slopes or curvature of the axial stress profiles does not remain the same. Distribution of transverse shear stress profile also depends on the metal–ceramic combination. Investigations on the static analyses of the FGM beams revealed that the deflections, stresses and the location of the neutral surface are highly dependent on power law index.

References

[1] M. Koizumi, FGM activities in Japan, Composites Part B 28B (1997) 1–4.
[2] R.K. Kapania, S. Raciti, Recent advances in analysis of laminated beams and plates, Part I: Shear effect and Buckling, AIAA J. 27 (7) (1989) 923–934.
[3] G. Shi, K.Y. Lam, T.E. Tay, On efficient finite element modeling of composite beams and plates using higher-order theories and an accurate composite beam element, Comput. Struct. 41 (1998) 159–165.
[4] A. Chakraborty, S. Gopalakrishnan, J.N. Reddy, A new beam finite element for the analysis of functionally graded materials, Int. J. Mech. Sci. 45 (2003) 519–539.
[5] B.V. Sankar, J.T. Tzeng, Thermal stresses in functionally graded beams, AIAA J. 40 (6) (2002) 1228–1232.
[6] B.V. Sankar, An elasticity solution for functionally graded beams, Comput. Sci. Technol. 61 (2001) 689–696.
[7] I. Calio, I. Elishakoff, Closed-form solutions for axially graded beam-columns, J. Sound Vibration 280 (2005) 1083–1094.
[8] L. Wu, Wang Qi-shen, I. Elishakoff, Semi-inverse method for axially functionally graded beams with an anti-symmetric vibration mode, J. Sound Vibration 284 (2005) 1190–1202.
[9] L.D. Croce, P. Venini, Finite elements for functionally graded Reissner–Mindlin plates, Comput. Methods Appl. Mech. Eng. 193 (2004) 705–725.
[10] A.M. Zenkour, Generalised shear deformation theory for bending analysis of functionally graded plates, Appl. Math. Model. 30 (2006) 67–84.
[11] Zhong Zheng, Yu Tao, Analytical solution of a cantilever functionally graded beam, Comput. Sci. Technol. 67 (2007) 481–488.
[12] H.J. Ding, D.J. Huang, W.Q. Chen, Elasticity solutions for plane anisotropic functionally graded beams, Int. J. Solids Struct. 44 (1) (2007) 176–196.
[13] A.M. Jiang, H.J. Ding, The analytical solutions for orthotropic cantilever beams (I): subjected to surface forces, J. Zhejiang Univ. Sci. 6A (2) (2005) 126–131.
[14] H.J. Ding, D.J. Huang, H.M. Wang, Analytical Solution for fixed-end beam subjected to uniform load, J. Zhejiang Univ. Sci. 6A (8) (2005) 779–783.
[15] S.Y. Oh, L. Librescu, O. Song, Thermoelastic modeling and vibration of functionally graded thin-walled rotating blades, AIAA J. 41 (10) (2003) 2051–2061.
[16] L. Librescu, S.Y. Oh, O. Song, Spinning thin-walled beams made of functionally graded materials: modeling, vibration and instability, Eur. J. Mech. A/Solids 23 (2004) 499–515.
[17] L. Librescu, S.Y. Oh, Thin-walled beams made of functionally graded materials and operating in a high temperature environment: vibration and stability, J. Therm. Stress. 28 (2005) 649–712.
[18] M. Deschilder, H. Eslami, Y. Zhao, Non-linear static analysis of a beam made of functionally graded material, in: 47th AIAA/ASME/ASCE/AHS/ASC Structures, Structural Dynamics, and Materials Conference, 1–4th May, Newport, RI, 2006.
[19] J.N. Reddy, C.D. Chin, Thermomechanical analysis of functionally graded cylinders and plates, J. Therm. Stress. 21 (1998) 593–626.
[20] P.R. Heyliger, J.N. Reddy, A higher order beam finite element for bending and vibration problems, J. Sound Vibration 126 (2) (1988) 309–326.
[21] C.Y.K. Chee, L. Tong, G.P. Steven, A mixed model for composite beams with piezoelectric actuators and sensors, Smart Mater. Struct. 8 (1999) 417–432.
[22] T.C. Mathew, G. Singh, G.V. Rao, Thermal buckling of cross-ply composite laminates, Comput. Struct. 42 (1992) 281–287.